IEEE Access
Multidisciplinary | Rapid Review | Open Access Journal

Received 21 June 2023, accepted 4 July 2023, date of publication 7 July 2023, date of current version 17 July 2023.

Digital Object Identifier 10.1109/ACCESS.2023.3293151

RESEARCH ARTICLE

Dynamic Characteristics Analysis of Double Pantograph Catenary of AC Rigid Catenary System

YING WANG[1,2], QIANG HUANG[1], XIAOQIANG CHEN[1,2], GANGHUI ZHAO[1], AND XIUQING MU[1]

[1]School of Automation and Electrical Engineering, Lanzhou Jiaotong University, Lanzhou 730070, China
[2]Key Laboratory of Opto-Technology and Intelligent Control Ministry of Education, Lanzhou 730070, China

Corresponding author: Qiang Huang (hqljdlt@163.com)

This work was supported in part by the National Natural Science Foundation of China Regional under Grant 52067013; and in part by the Natural Science Key Foundation of Gansu Provincial Department of Science and Technology under Grant 21JR7RA280, Grant 22JR5RA318, and Grant 22JR11RA162.

ABSTRACT The Euler-Bernoulli beam theory is used to establish the vibration differential equation of the rigid catenary, the cantilever support device is equivalent to the spring, and the pantograph is equivalent to the three mass block model. The double-pantograph-catenary (DPC) dynamic coupling model is established by using the penalty function, and utilize Newmark-β solved the model, verifying the reliability of the model with the field test contact forces of the rigid catenary system (RCS) of Xi'an Metro in China, and illustrating the vibration characteristics and fluctuation propagation characteristics of the rigid catenary structure in combination with the fluctuation propagation theory of beam and the sag model of rigid catenary. Based on the model, the dynamic interaction mechanism between the pantograph and the rigid catenary is studied, including the influence of different spans, speeds on the dynamic contact force of the DPC, the flow field of the pantograph is analyzed with ANSYS, and the influence of train induced wind in the tunnel is studied in combination with the DPC model. The results show that when the train operates on RCS with a double pantograph, the contact force fluctuation of the trailing pantograph (TP) is more severe than that of the leading pantograph (LP); Among the three common spans of 6m, 8m, and 10m, when the speed is less than 80 km/h, the span of 8m or 10m should be selected, when the speed is 80-140 km/h, the span of 6m or 8m should be selected, when the speed is greater than 140 km/h, the span should be the minimum 6m; With the increase of the wind velocity and the angle of attack, the fluctuation of the pantograph-catenary contact force of the RCS increases, and compared to the LP, the contact force fluctuation of the TP is greater.

INDEX TERMS Rigid catenary, double pantograph-catenary, vibration differential equation, speed, span.

NOMENCLATURE

DPC	double-pantograph-catenary.
RCS	rigid catenary system.
LP	leading pantograph.
TP	trailing pantograph.

The associate editor coordinating the review of this manuscript and approving it for publication was Jesus Felez.

I. INTRODUCTION

The overhead catenary is the transmission channel for electric energy in electrified railways. According to different structural forms, the overhead catenary can be divided into flexible catenary and rigid catenary [1]. The AC flexible catenary, most commonly used in electrified railways [2], is a distributed open-air elastic cable system [3], and the DC rigid catenary is used mostly in urban metro systems [4] due to its significant advantages in tunnels. But with the increase of train speed, the requirements for dynamic

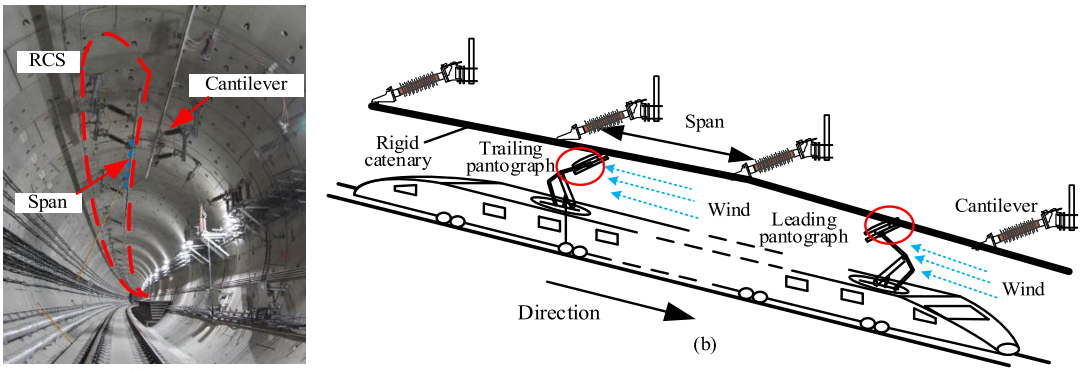

FIGURE 1. DPC model of RCS. (a) real RCS; (b) DPC structure.

contact performance between pantograph and catenary are higher [5], and the performance of rigid catenary is inferior at high speed [6]. Internationally the highest running speed of rigid catenary system (RCS) is recorded at 230 km/h on the Vienna-Linz intercity railway [7], in China, the maximum design speed of China's RCS is 160 km/h [8]. At present, the Sichuan-Tibet Railway with a design speed of 200 km/h has started construction. However, the proportion of tunnels along the Sichuan Tibet Railway is over 85%, and in tunnel section, rigid catenary has significant advantages over flexible catenary, such as large load capacity, fewer parts and small headroom. Therefore, it is advisable to use RCS for the Sichuan Tibet Railway. However, the current application of DC rigid catenary in short-distance cannot provide sufficient experience for the design of AC rigid catenary in the Sichuan Tibet Railway of long-distance and complex environments.

The dynamic performance of the pantograph and rigid catenary is the key factor for the reliable current collection of the train, it is also one of the important aspects that limit the speed of trains [8], studied through simulation modeling, [9] establishes a linear simulation model for RCS based on the absolute node coordinate method. Reference [10] proposed a finite element model for the transition section of an RCS. Reference [11] establishes the partial differential equation of rigid catenary. Reference [12] uses the finite element method to establish the dynamic model of pantograph and rigid catenary. Reference [9] establishes the model for transitioning from rigid catenary to flexible catenary. Reference [13] respectively used modal method and finite element method to establish a plane dynamic model and a spatial dynamic model of the RCS. Reference [14] A catenary transition device has been proposed to reduce contact losses between components when the speed exceeds a known limit. Reference [15] proved that there are some differences in the dynamic characteristics of different pantograph through the pantograph catenary simulation model. Reference [16] The dynamic current collection characteristics of the pantograph catenary system under the current collection mode of double pantograph are studied. Reference [1] A new and general analysis model of dynamic interaction between pantograph and catenary is proposed. In [17], the influence of the arc between the rigid catenary and the pantograph slide on the current during train operation was studied. In [18], a new type of rigid wire suitable for high-speed operation was developed. Reference [19] Conduct modal analysis and harmonic response analysis on various models of the pantograph. Reference [20] The influence of pantograph catenary structure parameters on the dynamic performance of pantograph and catenary is studied by using finite element model. And when the contact force between the pantograph and the catenary fluctuates in a large range, it will deteriorate the current collection quality of the train [21], [22]. Excessive contact force between pantograph and contact line will lead to excessive wear; The decrease in contact force will lead to arcing and cause local surface melting of the pantograph mesh. The mechanical wear and surface melting of the contact line and pantograph have changed the flatness of the contact surface, thus aggravating the deterioration of the current collection quality of the train and limiting the running speed of the train [23].

In the above work, with DC rigid catenary and single pantograph of urban rail transit as the main focus, the key parameters for modeling the AC rigid catenary modeling and the influencing factors of fluctuations during the operation of double pantographs are still unclear now. Usually, urban rail transit operates at low-speeds, and the impact of the train induced wind during high-speed operation has not been considered in the study of rigid catenary mentioned above. Therefore, as shown in Fig.1, this study has established the double-pantograph-catenary (DPC) model of RCS, through the analysis of the vibration differential equation of the rigid catenary. Combining the fluctuation propagation theory of beams and the sag model of beams, the fluctuation propagation and vibration characteristics of rigid catenary are elaborated, combining flow field analysis, analyze the dynamic performance of the pantograph-catenary under the influence of train induced wind at high-speeds, and improved the accuracy of RCS simulation.

II. ESTABLISHING DIFFERENTIAL EQUATIONS

The rigid catenary has a much smaller cross-section than the length, so the rigid catenary can be equated to an

Euler-Bernoulli beam, and the vibration differential equation for the Euler-Bernoulli beam is established.

A. VIBRATION DIFFERENTIAL EQUATIONS

Let the material density of the rigid catenary be ρ, the cross-sectional area is S, and the acting load is $f(x,t)$, as shown in Fig.2, a micro-element of thickness dx taken at any point, when bending vibration in the plane, the transverse displacement along the z-axis is the deflection of the beam is $w(x,t)$, the angle of rotation after vibration deformation is θ. The calculated moment for the integral within the cross-section is (1)

$$M = -EI\frac{\partial\theta}{\partial x} \tag{1}$$

In (1), E is the modulus of elasticity of the material, $I = bh^3/12$ is the secondary moment of the beam section, and b and h are the width and height of the beam section rectangle.

In small deflection conditions the angle of rotation is equal to the slope of the central axis of the beam after deformation, is (2)

$$\theta = \frac{\partial w}{\partial x} \tag{2}$$

Substituting (2) into (1), can be obtained (3)

$$M = -EI\frac{\partial^2 w}{\partial x^2} \tag{3}$$

The bending moment of the beam is proportional to the slope of the central axis, and EI is the bending stiffness of the beam; the force balance equation of the micro-element along the z-axis is listed according to D'Alembert's principle is (4)

$$(Fs + \frac{\partial w}{\partial x}dx) - Fs - \rho S(x)\frac{\partial^2 w}{\partial x^2}dx + f(x,t)dx = 0 \tag{4}$$

Moment of inertia from cross-sectional rotation is (5)

$$(M + \frac{\partial M}{\partial x}dx) - M - Fsdx + f(x,t)\frac{(dx)^2}{2} = 0 \tag{5}$$

omitting the quadratic term of dx

$$Fs = \frac{\partial M}{\partial x} \tag{6}$$

Substituting (3) and (6) into (4), gives (7)

$$\frac{\partial^2}{\partial x^2}\left[EI(x)\frac{\partial^2 w(x,t)}{\partial x^2}\right] + \rho S(x)\frac{\partial^2 w(x,t)}{\partial t^2} = f(x,t) \tag{7}$$

The rigid catenary is assumed to be of equal cross-section and simplified to (8)

$$EI\frac{\partial^4 w(x,t)}{\partial x^4} + \rho S\frac{\partial^2 w(x,t)}{\partial t^2} = f(x,t) \tag{8}$$

The action load of the rigid catenary contains two parts: contact force of pantograph-catenary $F_c(x,t)$ and gravity load of rigid catenary ρSg. The contact force is related to the contact point of pantograph catenary, the gravity load is applied along the continuous beam distribution and the stiffness of the

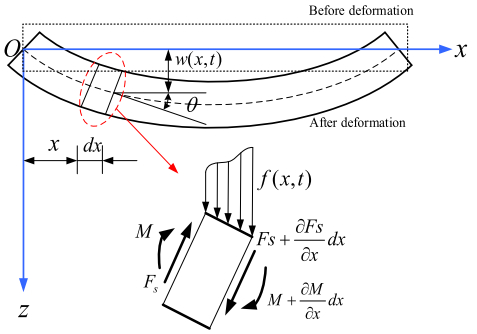

FIGURE 2. Force diagram of the Euler-Bernoulli beam for a micro-element.

TABLE 1. Parameters of the euler-bernoulli beam for a micro-element.

Parameters	Value	Parameters	Value
EI	216 000 Pa	g	9.8 m/s
ρ	5.9 kg/m	S	2198 mm^2
k_d	5×10^6 N/m	dx	0.01 m

rigid catenary is set to k_d, the related action force is expressed by the Dirac function. Specifically, this can be expressed as (9)

$$EI\frac{\partial^4 w(x,t)}{\partial x^4} + \rho S\frac{\partial^2 w(x,t)}{\partial t^2} + \sum_{j=1}^{m} k_d w(x,t)\delta(x - x_j) = F_c(x,t)\delta(x - x_t) + \rho Sg \tag{9}$$

The parameters of the Euler-Bernoulli beam for a micro-element of rigid catenary are shown in Table 1.

B. ANALYSIS OF DIFFERENTIAL EQUATIONS

The vibration differential equation (9) for rigid catenary is a fourth order partial differential equation, which is calculated analytically using the assumed modal method, and the expression for the vertical displacement $y(x,t)$ of the beamis set as (10)

$$y(x,t) = \sum_{i=1}^{NM}\varphi_i(x)q_i(t) \tag{10}$$

In (10), x, t are the horizontal displacement variables and the motion time variables respectively; $\varphi_i(t)$ are the canonical vibration functions of the assumed modes, see equation (11); $q_i(t)$ are the generalised coordinates; and NM are the modal truncation orders.

$$\varphi_i(x) = \sqrt{\frac{2}{\rho AL}}\sin(\frac{i\pi x}{L}) \tag{11}$$

Substituting (10) into (9) gives (12)

$$\sum_{i=1}^{NM}\rho S\varphi_i(x)\ddot{q}_i(t) + \sum_{i=1}^{NM}EI\frac{d^4\varphi_i(x)}{dx^4}q_i(t) + \sum_{j=1}^{m}k_d\delta(x - x_j)\sum_{i=1}^{NM}\varphi_i(x)q_i(t)$$

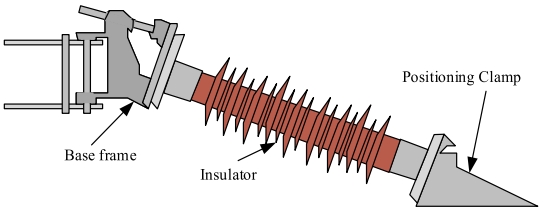

FIGURE 3. The structure of the Cantilever support device.

$$= F_c(x,t)\delta(x-x_t) + \rho Sg \tag{12}$$

According to the orthogonality of the regular oscillatory function, the left and right sides of (12) are multiplied by the same product partition function and decoupled to obtain (13)

$$\begin{aligned}&\ddot{q}_i(t) + \frac{EI}{\rho S}(\frac{i\pi}{L})^4 q_i(t)\\ &\quad + \sum_{j=1}^{m} k_d \varphi_h(x_j) \sum_{i=1}^{NM} \varphi_i(x_j) q_i(t)\\ &= F_c(x_0,t)\varphi_j(x_0) + \frac{\rho SgL}{h\pi}(\cos(h\pi) - 1)\end{aligned} \tag{13}$$

Expand (13) into matrix form as (14), shown at the bottom of the page.

III. MODELING OF DPC

Based on the vibration differential equations of a rigid catenary, DPC model of RCS can be established, and the interaction of pantograph-catenary and cantilever support device can be considered.

A. MODELING OF CANTILEVER SUPPORT DEVICE

As shown in Fig.1 (b), the cantilever support device (Fig.3) is used to fix the rigid catenary, which is composed of insulator, base frame, and positioning clamp composition. According to mechanical theory, the insulators can be simplified as a cantilever beam model with a concentrated mass at the free end, As shown in Fig.4 (a).

According to the theory of material mechanics, the combined deformation of cantilever beam at the free end is caused by the equivalent concentrated force mg of the insulator and the positioning clamp, and the distributed load of the insulator. When the free end is subjected to a bending force mg, the

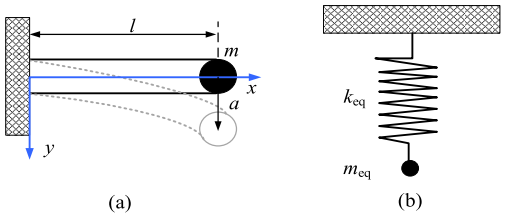

FIGURE 4. The mechanical model of Cantilever. (a) the simplified model of insulator; (b) the simplified model of cantilever.

displacement of the free end is (15):

$$x = \frac{mgl^3}{3E_bI_b} \tag{15}$$

In (15), mg is the equivalent concentrated force, E_bI_b is the bending stiffness of the beam, and l is the length of the beam, so the equivalent stiffness k_b of the cantilever beam is (16)

$$k_b = \frac{F}{x} = mg \Big/ \frac{mgl^3}{3E_bI_b} = \frac{3EI}{l^3} \tag{16}$$

Reference [32], the equivalent mass m of the cantilever beam as (17):

$$m_b = 0.2357\rho_b^2 l \tag{17}$$

In (17), ρ_b Is the density of the cantilever beam, and l is the length of the cantilever beam.

Equivalent the positioning clamp to a spring with a stiffness of k_p, the equivalent mass of the rigid catenary at the positioning point is m_p, because the equivalent point displacement of the cantilever beam is consistent with the displacement of the positioning clamp, Therefore, after connecting k_b and k_P in series, The equivalent stiffness of the cantilever support device is (18).

$$k_{eq} = \frac{k_b k_p}{k_b + k_p} \tag{18}$$

The equivalent mass of the cantilever support device is (19).

$$m_{eq} = m_p + 0.2357\rho_b^2 l \tag{19}$$

As shown in Fig.4(b), the simplified model of cantilever support device has equivalent stiffness $k_{eq} = 6.7 \times 10^7$N/m and equivalent mass m_{eq} =2.77kg.

$$\begin{bmatrix} 1 & \cdots & 0 \\ \vdots & \ddots & \vdots \\ 0 & \cdots & 1 \end{bmatrix} \begin{Bmatrix} \ddot{q}_1(t) \\ \vdots \\ \ddot{q}_{NM}(t) \end{Bmatrix} + \begin{bmatrix} \frac{EI}{\rho S}(\frac{\pi}{L})^4 + \frac{2}{\rho SL}\sum_{j=1}^{m} k_d \sin(\frac{\pi x_j}{L})\sin(\frac{\pi x_j}{L}) & \cdots & \frac{2}{\rho SL}\sum_{j=1}^{m} k_d \sin(\frac{\pi x_j}{L})\sin(\frac{NM\pi x_j}{L}) \\ \vdots & \ddots & \vdots \\ \frac{2}{\rho SL}\sum_{j=1}^{m} k_d \sin(\frac{NM\pi x_j}{L})\sin(\frac{\pi x_j}{L}) & \cdots & \frac{EI}{\rho S}(\frac{NM\pi}{L})^4 + \frac{2}{\rho SL}\sum_{j=1}^{m} k_d \sin(\frac{NM\pi x_j}{L})\sin(\frac{NM\pi x_j}{L}) \end{bmatrix}$$

$$\cdot \begin{Bmatrix} q_1(t) \\ \vdots \\ q_{NM}(t) \end{Bmatrix} = \frac{\rho gSL}{\pi}\sqrt{\frac{2}{\rho SL}} \begin{Bmatrix} -2 \\ \vdots \\ \frac{-2}{NM} \end{Bmatrix} + F_c(x_0,t)\sqrt{\frac{2}{\rho SL}} \begin{Bmatrix} \sin(\frac{\pi(x_0+vt)}{L}) \\ \vdots \\ \sin(\frac{NM\pi(x_0+vt)}{L}) \end{Bmatrix} \tag{14}$$

B. MODELING OF DOUBLE PANTOGRAPHS

For the DPC model of RCS, The pantograph is simulated by the three-mass block model, as shown in Fig.5, $m_1 \sim m_3$ is the equivalent mass of head, upper frame and lower frame of pantograph respectively, $k_1 \sim k_3$ is the equivalent spring stiffness of head, upper frame and lower frame of pantograph respectively, $c_1 \sim c_3$ is the equivalent damping of head, upper frame and lower frame of pantograph respectively, $y_{l1} \sim y_{l3}$ and $y_{t1} \sim y_{t3}$ denote the vertical displacement of each mass block of leading pantograph (LP) and trailing pantograph (TP) respectively; $\dot{y}_{l1} \sim \dot{y}_{l3}$ and $\dot{y}_{t1} \sim \dot{y}_{t3}$ denote the vertical velocity of each mass block of LP and TP respectively; $\ddot{y}_{l1} \sim \ddot{y}_{l3}$ and $\ddot{y}_{t1} \sim \ddot{y}_{t3}$ denote the vertical acceleration of each mass block of LP and TP respectively; F_{cl}, F_{ct}, F_{0l} and F_{0t} denote the contact force of pantograph-catenary and the lifting force acting on the lower frame of the LP and TP respectively. Therefore, the vibration equation of the double-pantograph can be expressed as (20).

$$M_p\ddot{y}_p + C_p\dot{y}_p + K_p y_p = F_p \tag{20}$$

where: $M_p = diag(M_{lp}, M_{tp})$, $C_p = diag(M_{lp}, M_{tp})$, $K_p = diag(M_{lp}, M_{tp})$, "$diag(\ldots)$" denotes the block diagonal matrix; $y_p = [y_{lp}; y_{tp}]$, $F_p = [F_{lp}; F_{tp}]$, the subscripts "lp" and "tp" denote the parameters of the LP and TP respectively. Where:

$$\begin{aligned}
M_{lp} = M_{tp} &= \begin{bmatrix} m_1 & 0 & 0 \\ 0 & m_2 & 0 \\ 0 & 0 & m_3 \end{bmatrix}, \\
C_{lp} = C_{tp} &= \begin{bmatrix} c_1 & -c_1 & 0 \\ -c_1 & c_1 + c_2 & -c_2 \\ 0 & -c_2 & c_2 + c_3 \end{bmatrix}, \\
K_{lp} = K_{tp} &= \begin{bmatrix} k_1 & -k_1 & 0 \\ -k_1 & k_1 + k_2 & -k_2 \\ 0 & -k_2 & k_2 + k_3 \end{bmatrix}, \\
y_{lp} &= \begin{bmatrix} y_{l1} \\ y_{l2} \\ y_{l3} \end{bmatrix}, \quad y_{tp} = \begin{bmatrix} y_{t1} \\ y_{t2} \\ y_{t3} \end{bmatrix},
\end{aligned} \tag{21}$$

$$F_{lp} = \begin{bmatrix} -F_{cl} \\ 0 \\ F_{0l} \end{bmatrix}, \quad F_{tp} = \begin{bmatrix} -F_{ct} \\ 0 \\ F_{0t} \end{bmatrix} \tag{22}$$

C. MODELING OF DPC

The DPC model of RCS is shown in Fig.5, and the sliding friction contact problem between the pantograph and the RCS is handled by a penalty function, and the LP and TP calculations are shown in (23) and (24) respectively

$$F_{cl}(t) = \begin{cases} k_c \triangle\kappa_l(t)\kappa_l & \triangle(t) > 0 \\ 0 & \triangle\kappa_l(t) \le 0 \end{cases} \tag{23}$$

$$F_{ct}(t) = \begin{cases} k_c \triangle\kappa_t(t)\triangle\kappa_t & (t) > 0 \\ 0 & \triangle\kappa_t(t) \le 0 \end{cases} \tag{24}$$

In (18) and (19), $F_{cl}(t)$ is the LP contact force at moment t, $F_{ct}(t)$ is the TP contact force at moment t, k_c is the contact stiffness between the pantograph and the RCS, as shown in Fig.5, the pantograph head penetrates into the contact wire of RCS, $\triangle\kappa_l(t)$ is the difference of the RCS displacement and the LP displacement, at the LP-catenary contact points at moment t; $\triangle\kappa_t(t)$ is the difference of the RCS displacement and the TP displacement, at the TP-catenary contact points at moment t. The LP and TP contact force is the product of the penetration displacement $\triangle\kappa_t(t)$ and $\triangle\kappa_l(t)$, and the contact stiffness k_c respectively; when the displacement of pantograph head is below the displacement of RCS, the pantograph-catenary contact force is 0.

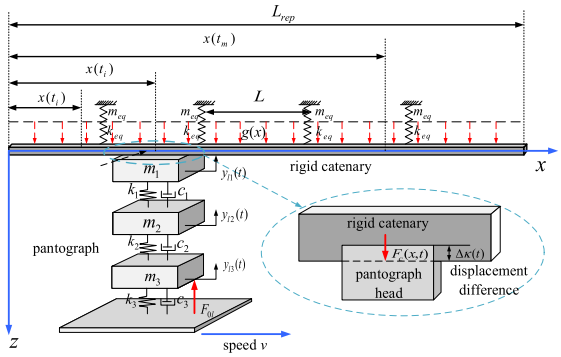

FIGURE 5. Calculation model of pantograph-catenary.

TABLE 2. Parameters of rigid catenary and pantograph.

Parameters	Value	Parameters	Value
k_c	50 000 N/m	m_2	5.855 kg
L	6~10 m	m_3	4.645 kg
NM	50	k_1	8 380 N/m
F_{0l}	90 N	k_2	6 200 N/m
F_{0t}	90 N	k_3	80 N/m
k_{eq}	6.7×10^7N/m	c_1	0 Ns/m
m_{eq}	2.77 kg	c_2	0 Ns/m
m_1	7.510 kg	c_3	70 Ns/m

Parameters of rigid catenary and pantograph are shown in Table 2.

D. SOLVING DYNAMIC MODEL

In summary, the DPC dynamics equations of the RCS have been given (14), (15), (17), (18) and (19), refer [28], using the Newmark-β to solve each ordinary differential equation, to derive the displacement and force of each pantograph-catenary contact points, it is can be obtained by the presented iteration procedure as follows.

Step1 Based on the parameters of rigid catenary in Table.2, establish the vibration differential equation according to (9), (10), (11), (12), and (13).

Step2 Calculate the equivalent stiffness of k_{eq} and equivalent mass m_{eq} according to (18) and (19).

Step3 Input the initial lifting force F_{0l} and F_{0t} of double pantographs.

Step4 Calculate the initial mass matrix, stiffness matrix, damping matrix and forces matrix at time t based on (14) and (20)

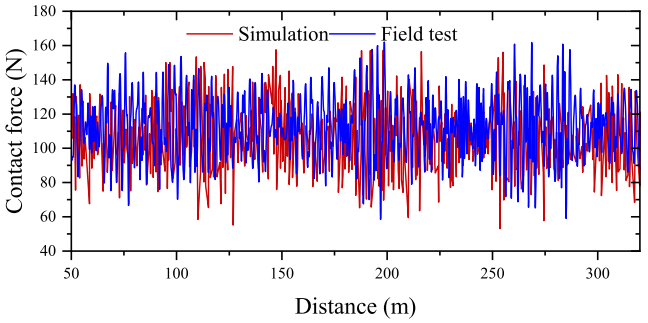

FIGURE 6. Contact forces from simulation and field test.

Step5 According to Newmark-β Calculate the displacement difference $\triangle\kappa_l(t)$ and $\triangle\kappa_t(t)$ of the contact point between the RCS and double pantograph.

Step6 Calculate the contact force $F_{cl}(t)$ and $F_{ct}(t)$ of the contact point DPC at time t according to (23) and (24).

Step7 If $t = L_{\text{rep}}/\text{v}$. If not, then $t = t+1$, and return to step 4. If so, end the calculation.

E. MODEL VALIDATION

In order to verify the reliability of the DPC model, compare the simulation contact forces of the model with the field test contact forces and the evaluation standard.

1) RCS FIELD TEST VALIDATION

The simulation LP contact forces of the DPC model are compared with the field test contact forces of Xi'an Metro in China at the speed of 140 km/h. comparison of contact force curves is shown in Fig.6.

The maximum contact force $F_{\max}$, average contact force F_{m}, minimum contact force $F_{\min}$, and standard deviation σ of the contact force within the range of 0-20 Hz for simulation and field test are shown in Table 4.

From Table 4, it can be seen that the contact force statistics obtained by numerical simulation show good consistency with the field test. The relative error of $F_{\max}$, F_{m}, and $F_{\min}$ is usually below 5%, and σ is only -7.52%.

2) RCS EVALUATION STANDARD VALIDATION

At present, the simulation and test of RCS in china generally adopt the relevant evaluation standards based on the IEC 62486-2017 standard of the international electrotechnical commission [26]. The relevant evaluation standards are shown in Table 1, from which it can be seen that the contact force of the pantograph-catenary is evaluated by the average F_{m}, the max $F_{\max}$, the min $F_{\min}$ and the standard deviation σ.

Comparing Table 3 and Table 4, it can be seen that LP contact force of simulation meets the acceptance threshold specified in the IEC 62486-2017 standard of the International Electrotechnical Commission, and according to the evaluation index in Table 3, the simulated LP contact forces $F_m - 3\sigma = 57.38N$ and $0.1F_m = 11.02N$, the simulated TP contact forces $F_m - 3\sigma = 52.76N$ and $0.1F_m = 11.21N$,meet the standard requirements of $F_m - 3\sigma > 0.1F_m$.

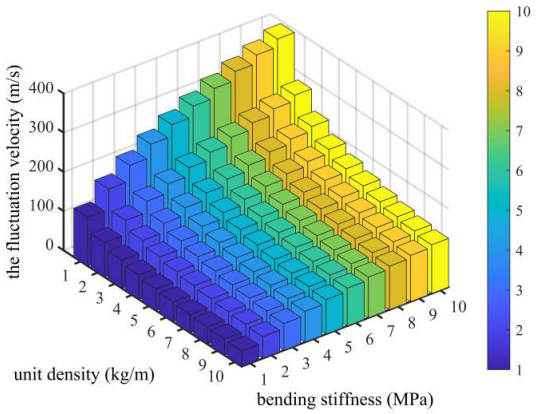

FIGURE 7. The relationship between THE fluctuation velocity, unit density and bending stiffness OF rigid catenary.

IV. DYNAMIC CHARACTERISTICS ANALYSIS OF DPC

A. INFLUENCE OF DOUBLE PANTOGRAPHS

The three mass block model parameters of different pantographs are also different, and the corresponding dynamic characteristics of pantograph-catenary are also different. Moreover, although the double pantograph operation greatly improves transportation efficiency, there is also a problem of increasing TP vibration [27], [31].

Double pantograph operation simultaneously, and the LP contact with the RCS generates contact forces and produces small fluctuations along the catenary propagation, small fluctuations make the TP-catenary dynamic coupling vibration intensified. Based on the differential equation of beam vibration and the plane harmonic equation, the fluctuation velocity v_u of rigid catenary can be derived (25)

$$v_u = \frac{\pi}{L}\sqrt{\frac{EI}{\rho S}} \tag{25}$$

From Fig.7, it can see that as the bending stiffness increases and the unit density decreases, the fluctuation velocity decreases.

B. INFLUENCE OF THE SPAN OF RIGID CATENARY

The span of RCS is the distance between two adjacent cantilever support devices [28], usually spanning 5-12m, and there are three common spans: 6m, 8m and 10m. The traditional view is that the span of RCS is related to the train speed, larger spans can be used for lower speeds, while smaller spans can be used for higher speeds [30].

1) ANALYSIS OF THE SPAN OF RIGID CATENARY

As shown in Fig.8, within a span, the two ends of the catenary are fixed by two cantilever support devices, in a stationary state, due to the weight of the rigid catenary, the rigid catenary within the span is not an absolute plane, but slightly bent. The vertical distance between the lowest point of the RCS within the span and the two suspension structures is called the relaxation degree f of the span, the relaxation

TABLE 3. Evaluation standard for dynamic performance of AC rigid catenary.

speed v/(km·h^{-1})	contact force F/N		average contact force F_m/N		evaluation index
	F_{max}	F_{max}	Minimum F_m	maximum F_m	
≤200	>0	300	$0.0047v^2$+60	$0.0047v^2$+90	$F_m - 3\sigma > 0.1F_m$
>200	>0	350	$0.0047v^2$+60	$0.0097v^2$+90	

TABLE 4. Contact force verification OF simulation and field test.

	Simulation (N)	Field test (N)	Error (%)
F_{max}	162.10	157.55	2.9
F_m	110.18	105.29	4.6
F_{min}	55.46	53.12	4.4
σ	17.60	19.10	-7.8

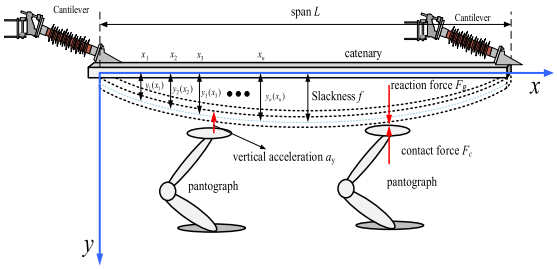

FIGURE 8. The sag model of rigid catenary.

degree f is (26)

$$f = \frac{\rho S L^4}{384EI} \tag{26}$$

As shown in Fig.8, The RCS is sinusoidal in shape within a span, take the plane parallel to the non relaxation rigid catenary as the x-axis and the downward vertical plane as the y-axis, the RCS sag model is as (27).

$$y = \frac{f}{2}\cos\frac{2x\pi}{L} \tag{27}$$

According to the mechanics balance principle, the contact force of the pantograph on the RCS is F_c, and the reaction force of the rigid catenary is F_R. Meanwhile, the pantograph has a vertical acceleration a_y, and the equivalent mass of the pantograph is expressed by m; the mechanical equilibrium equation can be obtained as (28)

$$ma_y = F_c - F_R \tag{28}$$

The pantograph running speed $v = \frac{dx}{dt}$, the pantograph vertical acceleration a_y is the second order derivative of the displacement in the y-axis direction $\frac{d^2y}{dt^2}$, which a_y can be derived as (29)

$$a_y = \frac{d^2y}{dt^2} = \frac{d^2y}{dt^2}\cdot\frac{d^2x}{d^2x} = \left(\frac{dx}{dt}\right)^2\cdot\frac{d^2y}{dx^2} = v^2\frac{d^2y}{dx^2} \tag{29}$$

During pantograph operation, the allowable pantograph-catenary pressure loss shall not exceed 12% of contact force F_c. Therefore, combining (27), (28), and (29) yields (30):

$$-mv^2\frac{f}{2}\left(\frac{2\pi}{L}\right)^2\cos\frac{2x\pi}{L} < 0.12F_c \tag{30}$$

Over eliminating the cosine function, the theoretical solution is obtained as (31):

$$L^2 < \frac{768\times 0.12F_cEI}{4\pi^2\rho m v^2} \tag{31}$$

Based on (31), the maximum theoretical value of the span for different speeds of the train can be obtained, see Fig.9.

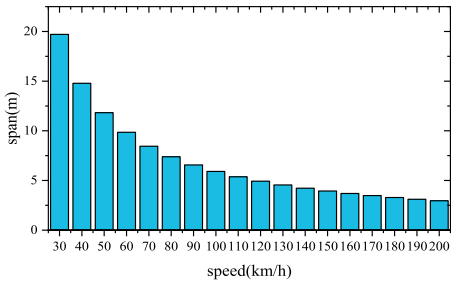

FIGURE 9. Maximum theoretical value of span at different speeds.

2) ANALYSIS OF TEST RESULTS

Simulation of pantographs at the three speed levels of 80km/h, 140km/h and 200km/h at 6m span, 8m span and 10m span, the simulation results are as follows.

It can be seen from Fig.10 that when the pantographs operates the RCS at the three speed levels of 80km/h, 140km/h and 200km/h, the contact force fluctuation of the 6m span is the smallest, followed by the 8m span, and the 10m span has the largest contact force fluctuation.

By comparing Fig. 10(a), (b) and (c) and Fig. 10(d), (e) and (f), it can be seen that the contact force fluctuation of the RCS gradually increases as the speed levels increases, and the fluctuation range of the LP is smaller than that of the TP at the same speed levels and span.

As can be seen from Fig.11(a), (d), (c) and (f), When the span is 6m and speeds are 80km/h and 200km/h, the contact force of LP and TP, that interquartile range 25%-75% and 1.5 IQR is the narrowest, followed by the next narrowest at 8m span and the most dispersed at 10m span. In particular, by comparing Fig.11(b) and Fig.11(e), it can be seen that at a speed level of 140km/h, the interquartile range 25%-75% of the contact forces, 1.5IQR is closer for the LP and TP operating at 10m span and 8m span, with the contact forces more concentrated for the TP at 10m span than at 8m span.

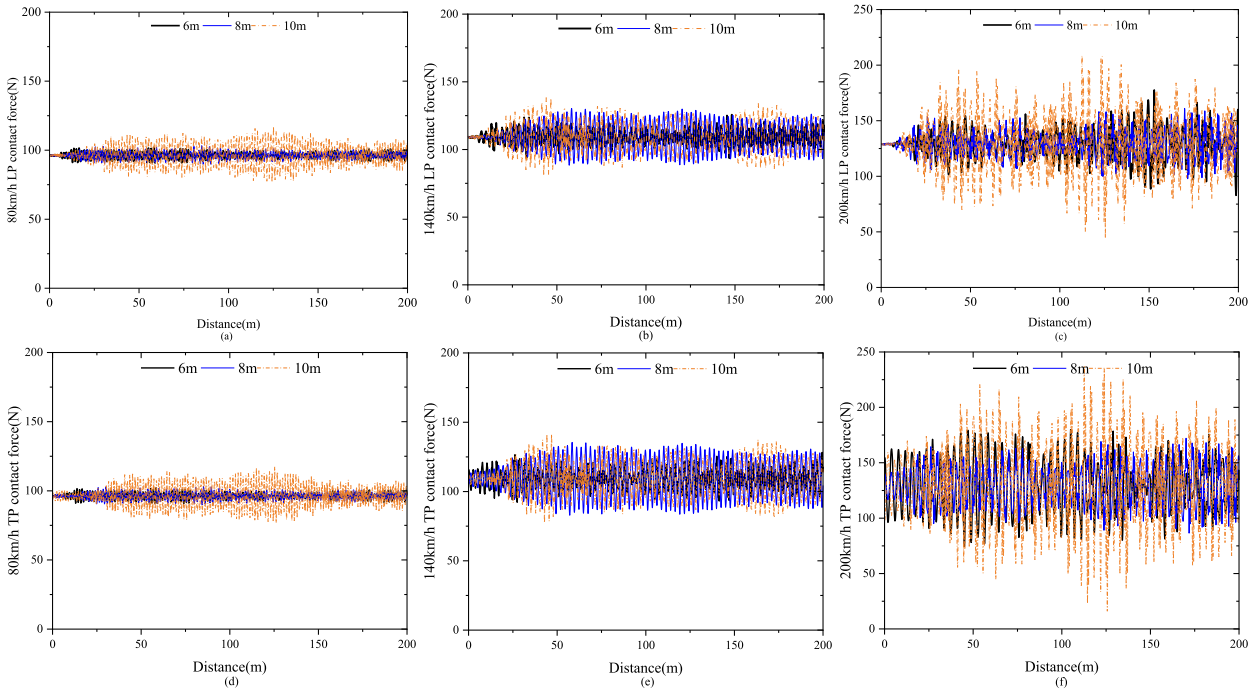

FIGURE 10. Contact forces between pantograph and RCS with three spans under three speeds.

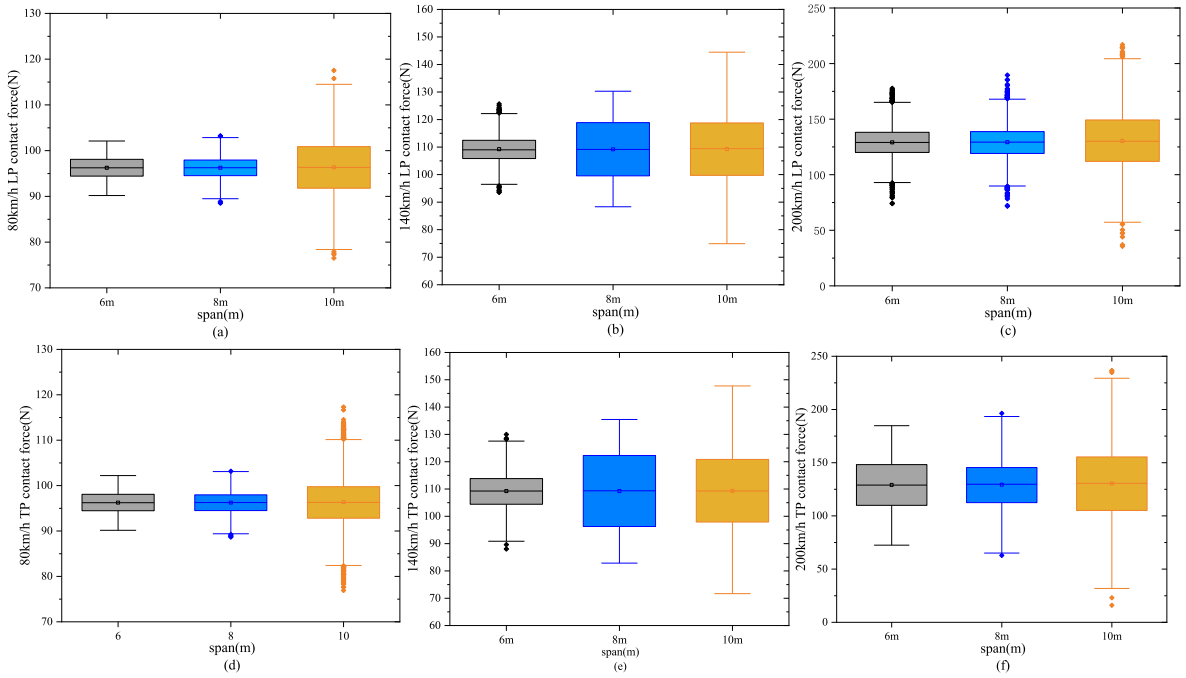

FIGURE 11. Box diagram of contact forces between pantograph and RCS with three spans under three speeds.

By comparing Fig.11 (a), (b), (c), (d), (e) and (f), it can be seen that the box diagram of 18 contact forces and RCS under three speed levels and three spans operation is symmetrical with respect to their respective the median lines, so the 18 contact forces are approximately subject to normal distribution. The average values of the LP and TP contact forces are around 97N, 110N and 130N respectively for the three speed levels. Therefore, when the train speed is less than 140km/h, the span of 6m and 8m can be selected. From a cost saving perspective, when the train speed is less than 80km/h, the span of 8m or 10m should be selected. When the operating speed is greater than 140km/h, the minimum span should be 6m.

C. INFLUENCE OF TRAIN INDUCED WIND

The RCS is arranged in the tunnel, and when the train runs at high-speed in the tunnel, the air flow is hindered by the

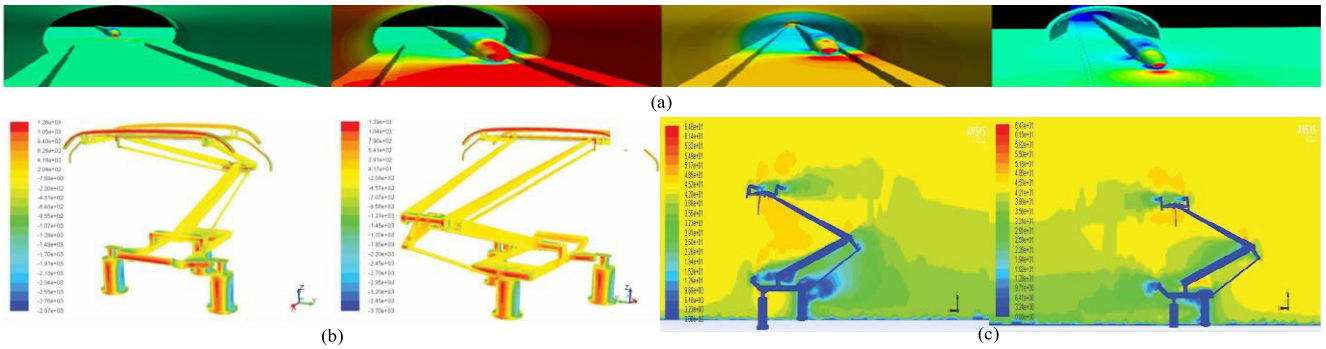

FIGURE 12. Cloud picture of pantograph at 160 km/h. (a) Air pressure caused by trains entering and exiting the tunnel (b) Static pressure when the pantograph opens and closes at 160 km/h (c) Flow velocity when the pantograph opens and closes at 160 km/h.

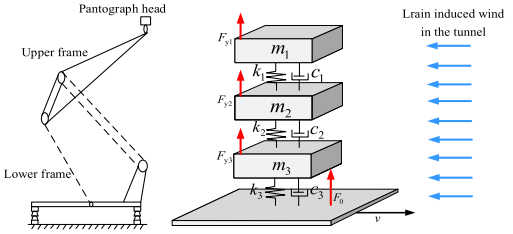

FIGURE 13. Air lifting force of pantograph under high-speed operation in tunnel.

limitations of the tunnel wall, causing severe compression of the static air at the front end of the train [29]. It is necessary to consider the influence of train induced wind in the tunnel on the coupling of rigid catenary and pantograph.

1) ANALYSIS OF TRAIN INDUCED WIND

The flow field of the pantograph in the tunnel was analyzed with ANSYS, the train speed is set at 160km/h, the cloud picture of pantograph at 160 km/h.

As shown in Figure 12 (a), it is a cloud map of tunnel air pressure caused by trains entering and exiting the tunnel and traveling inside the tunnel. It can be seen from Fig.12 (b), at 160km/h, the maximum static pressure on the surface of the pantograph under the closed working condition is greater than the maximum static pressure on the surface of the pantograph under the open working condition. The closed working condition is about 2% higher than the open working condition. The maximum static pressure on the surface of the pantograph is located on the windward side of pantograph head, lower frame, the minimum static pressure on the surface of the pantograph under the closed working condition is also less than the minimum static pressure on the surface of the pantograph under the open working condition. The closed working condition is 25%∼35% less than the open working condition. The minimum static pressure on the surface of the pantograph is mainly located on both sides of the insulator.

It can be seen from Fig.12 (c), at 160km/h, the flow velocity near the head and upper frame of the pantograph is significantly higher than that near the lower frame, and the maximum flow velocity is near the pantograph head. The maximum velocity near the pantograph head in the simulation flow field is about 45% higher than the set value, especially at the pantograph head, is much higher than the running speed of the train, which also shows that its working conditions are quite bad.

In the process of high-speed operation of the train, the pantograph is subjected to horizontal and vertical aerodynamic forces, and the horizontal force has little impact on the contact force of pantograph-catenary, so only the air lifting force on the pantograph in the vertical direction is considered. As shown in Fig.13, the air lift force on the pantograph is the sum of the surface air friction force and differential pressure lift force in the vertical direction.

The air lifting force of the lower frame of pantograph under the train induced wind action is as shown in (32)

$$\begin{aligned} F_{y1} &= (F'_{y1} + F''_{y1})L_1 \\ &= \Big\{2\pi\rho_a C\,|V_\infty|^2(\sin^2\theta_\infty\cos\theta_\infty + \cos^2\theta_\infty\sin\theta_\infty) \\ &\quad + \frac{1}{2}\rho_a\,|V_\infty|^2\,C_{d1}(X_c\sin^2\theta_\infty\cos\theta_\infty \\ &\quad - Y_c\cos^2\theta_\infty\sin\theta_\infty)\Big\}L_1 \end{aligned} \tag{32}$$

In (32), F'_{y1} is the lifting force generated by the surface pressure of the pantograph head, F''_{y1} is the lifting force of the pantograph head pressure difference resistance in the vertical direction, L_1 is the length of the pantograph skateboard, X_c is the width of the pantograph skateboard, Y_c is the thickness of the pantograph skateboard, V_∞ is the train induced wind velocities, θ_∞ is the angle of train induced wind velocities, C_{d1} is the resistance coefficient of the pantograph skateboard, ρ_a is the air mass density, and C is a specific constant.

The air lifting force of the upper frame of pantograph under the train induced wind action is as shown in (33)

$$\begin{aligned} F_{y2} = (F'_{y2}+F''_{y2})L_2 = \Big\{&-4\pi\rho_a r_1\,|V_\infty|^2\sin^2\theta_\infty\sin^2\alpha\cos\alpha \\ &+\rho_a r_1\,|V_\infty|^2\,C_{d2}\sin^2\alpha\cos\alpha\Big\}L_2 \end{aligned} \tag{33}$$

In (33), F'_{y2} is the lifting force generated by the surface pressure of the upper frame of pantograph, F''_{y2} is the upper frame lifting force of the pressure difference resistance in the vertical direction, L_2 is the length of the upper frame of pantograph, α is the angle of the upper frame of pantograph, C_{d2}

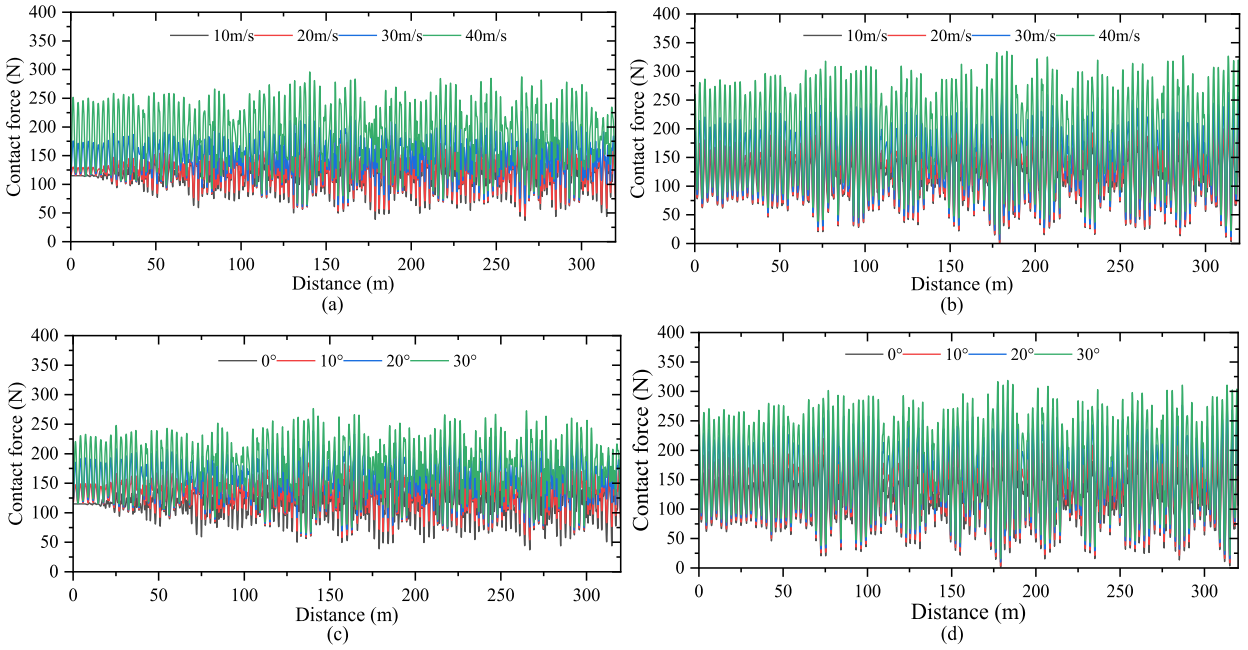

FIGURE 14. Simulation results. (a) Contact forces of LP at four wind velocities. (b) Contact forces of TP at four wind velocities. (c) Contact forces of LP at four wind attack angles. (d) Contact forces of TP at four wind attack angles.

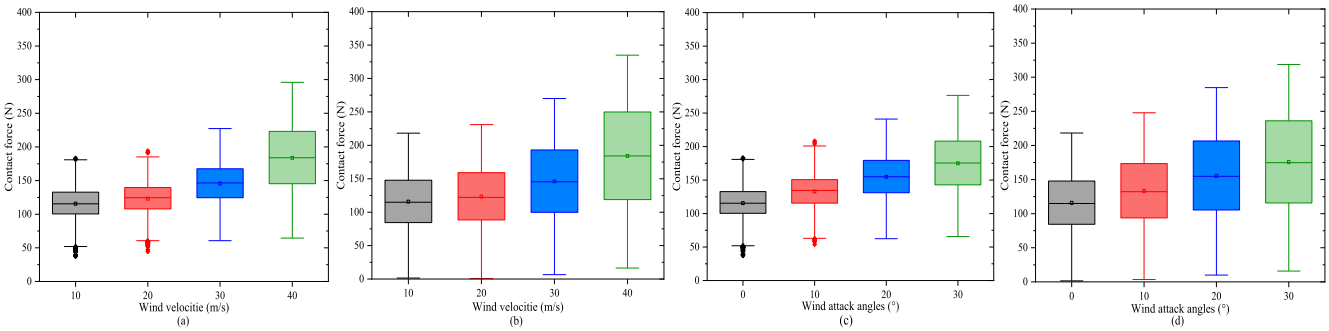

FIGURE 15. Box diagram of contact force. (a) Contact forces of LP at four wind velocities. (b) Contact forces of TP at four wind velocities. (c) Contact forces of LP at four wind attack angles. (d) Contact forces of TP at four wind attack angles.

is the resistance coefficient of the upper frame of pantograph, r_2 is the radius of the circular section of the upper frame.

The air lifting force of the lower frame of pantograph under the train induced wind action is as shown in (34)

$$F_{y3} = (F'_{y3} + F''_{y3})L_3 = \left\{ -4\pi\rho_a r_2 |V_\infty|^2 \sin^2\theta_\infty \sin^2\beta\cos\beta + \rho_a r_2 |V_\infty|^2 C_{d2} \sin^2\beta\cos\beta \right\} L_3 \quad (34)$$

In (34), F'_y is the lifting force generated by the surface pressure of the lower frame of pantograph, F''_y is the lower frame lifting force of the pressure difference resistance in the vertical direction, L_3 is the length of the lower frame of pantograph, β is the angle of the lower frame of pantograph, C_{d3} is the resistance coefficient of the lower frame of pantograph, r_2 is the radius of the circular section of the lower frame.

2) ANALYSIS OF TEST RESULTS

Four wind velocities of 10m/s, 20m/s, 30m/s, and 40m/s were selected for simulation under conditions of wind attack angle of 10° and train speed of 160km/h, and four wind attack angles of 0°, 10°, 20° and 30° were selected for simulation at wind velocity of 10m/s and train speed of 160 km/h. The simulation results are shown in Fig.14.

As can be seen from Fig.14, It can be seen that with the increase of the wind velocities and the wind attack angles at the train speed of 160 km/h, the fluctuation of the pantograph-catenary contact force of the RCS increases, and the fluctuation range of the TP is greater than that of the LP for all three pantographs operating with DPC, which is consistent with the fluctuation propagation theory of the rigid catenary.

From Fig.15, it can be seen that at the train speed of 160km/h, wind attack angle greater than 10°, and wind velocity greater than 10m/s, as the wind velocity and wind attack angle increase, the contact force of 25%-75%, average value, median value and 1.5IQR increases, and TP contact force is 25%-75%, 1.5IQR wider than LP contact force.

By comparing Fig.15 (a), (b) and Fig.15 (c), (d), it can be seen that the box line diagrams of the sixteen contact forces are all symmetrical with respect to the median line, which

means that the contact forces approximately obey a normal distribution, From Fig.15 (a), (b), it can be seen that the average values of TP and LP are around 115.54N, 132.98N, 154.94N and 175.12N at wind velocities of 10m/s, 20m/s, 30m/s and 40m/s. In addition, in Fig.15 (b), when the wind attack angle is 10°, the wind velocities are 10 m/s and 20 m/s, the minimum contact force of TP is 0, which mean that the pantograph is not in contact with the rigid catenary at this moment. From Fig.15 (c), (d), it can be seen that the average values of TP and LP are around 115.54N, 123.02N, 145.79N and 183.75N at wind attack angles of 0°, 10°, 20° and 30°. In addition, in Fig.15 (d), when the wind velocities is 10m/s, the wind attack angle is 0°, the minimum contact force of TP is 0, which mean that the pantograph is not in contact with the rigid catenary at this moment.

V. CONCLUSION

In this paper, a DPC dynamic coupling model of RCS is established, and verify the reliability of the DPC model using the field test contact forces from Xi'an Metro and evaluation standards, The model focuses on the vibration characteristics and double pantograph catenary propagation characteristics of AC rigid catenary. The conclusion is as follows:

According to the fluctuation propagation theory of beams, the LP coupled with the rigid catenary generates fluctuations of catenary, resulting in increased vibration of the TP, at the same time, the simulation shows that the contact force fluctuation of the TP is more intense than that of the LP under same speed classes and same span conditions.

Combined with the sag model of rigid catenary, the selection of span is related to the train speed, among the spans of 6m, 8m, and 10m, when the train speed is less than 80 km/h, the span of 8m or 10m should be selected, when the train speed is 80-140 km/h, the span of 6m or 8m should be selected,, when the train speed is greater than 140 km/h, the span should be the minimum 6m.

According to the flow field analysis, when the pantograph runs at a high-speed in the tunnel, the three main parts of the pantograph head, upper frame and lower frame are affected by the air flow. The train induced wind in the tunnel is combined with the DPC dynamic coupling model of RCS for simulation. The results show that with the increase of wind speeds and attack angles, the fluctuation of the contact force increases.

Now, on the basis of the model established in this paper, the dynamic interaction mechanism between the pantograph and the rigid catenary has been studied. In the future, more accurate verification will be carried out using field test data from double pantograph and field test data at multiple speed levels.

ACKNOWLEDGMENT

The authors would like to thank the engineers from China Xi'an Metro who assisted in the field test.

REFERENCES

[1] E. Karakose, M. T. Gencoglu, M. Karakose, I. Aydin, and E. Akin, "A new experimental approach using image processing-based tracking for an efficient fault diagnosis in pantograph–catenary systems," *IEEE Trans. Ind. Informat.*, vol. 13, no. 2, pp. 635–643, Apr. 2017.

[2] X. Chen, Z. Xi, Y. Wang, and X. Wang, "Improved study on the fluctuation velocity of high-speed railway catenary considering the influence of accessory parts," *IEEE Access*, vol. 8, pp. 138710–138718, 2020.

[3] J. Zhang, H. Zhang, B. Song, S. Xie, and Z. Liu, "A new active control strategy for pantograph in high-speed electrified railways based on multi-objective robust control," *IEEE Access*, vol. 7, pp. 173719–173730, 2019.

[4] F. Guo, X. Wang, J. Kou, F. Li, and C. Han, "Impact of surface roughness on pantograph-catenary current collection quality," *IEEE Access*, vol. 10, pp. 93951–93959, 2022.

[5] S. Wang and X. Li, "Vibration characteristics analysis and structure optimization of catenary portal structure on four-wire bridge," *Struct. Durability Health Monit.*, vol. 16, no. 4, pp. 361–382, 2022.

[6] Y. Wang, Z. Liu, X. Mu, K. Huang, H. Wang, and S. Gao, "An extended Habedank's equation-based EMTP model of pantograph arcing considering pantograph-catenary interactions and train speeds," *IEEE Trans. Power Del.*, vol. 31, no. 3, pp. 1186–1194, Jun. 2016.

[7] A. Oya, M. Shimizu, T. Mandai, K. Nishi, and M. Tago, "Application of overhead rigid conductor line to mountain tunnel of conventional lines," Presented at the IEEE Int. Conf. Ind. Technol., Hong Kong, Dec. 2005.

[8] G. He, "Research progress and prospect of 160 km/h overhead rigid catenary technology," *Eng. Construct. Des.*, vol. 19, pp. 131–134, Oct. 2022.

[9] L. Chen, F. Duan, Y. Song, Z. Hu, Z. Liu, and X. Feng, "Assessment of dynamic interaction performance of high-speed pantograph and overhead conductor rail system," *IEEE Trans. Instrum. Meas.*, vol. 71, pp. 1–14, 2022.

[10] A. Bautista, J. Montesinos, and P. Pintado, "Dynamic interaction between pantograph and rigid overhead lines using a coupled FEM—Multibody procedure," *Mech. Mach. Theory*, vol. 97, pp. 100–111, Mar. 2016.

[11] J. Guan and J. Wu, "Numerical solution of dynamic coupling equation between pantograph and rigid catenary," *J. Railway Sci. Eng.*, vol. 13, no. 2, pp. 362–368, Feb. 2016.

[12] K. Li and J. Guan, "Simulation study on strength matching of rail transit overhead rigid catenary," *Comput. Simul.*, vol. 36, no. 8, pp. 145–150 and 297, Aug. 2019.

[13] Y. Song, Z. Liu, A. Rønnquist, P. Navik, and Z. Liu, "Contact wire irregularity stochastics and effect on high-speed railway pantograph–catenary interactions," *IEEE Trans. Instrum. Meas.*, vol. 69, no. 10, pp. 8196–8206, Oct. 2020.

[14] J. Guan, Z. Tian, and J. Wu, "Research of 160 km/h transition structure proposal between overhead conductor rail and contact line based on dynamic simulation," *J. China Railway Soc.*, vol. 40, no. 9, pp. 48–56, Sep. 2018.

[15] J. D. D. S. Bobi, A. BerbeyAlvarez, A. Calvo-Hernadez, and J. Guevara-Cedeño, "Characterization of the dynamic behavior of transition systems between rigid and flexible catenary," Presented at the 7th Int. Eng., Sci. Technol. Conf. (IESTEC), Panama, Panama, Oct. 2019.

[16] X. Zhang and X. Chen, "Dynamic characteristic analysis of double-pantograph-catenary system of long marshalling EMU," Presented at the IEEE 5th Inf. Technol. Mechatronics Eng. Conf. (ITOEC), Chongqing, China, Jun. 2020.

[17] S. Bruni, G. Bucca, M. Carnevale, A. Collina, and A. Facchinetti, "Pantograph–catenary interaction: Recent achievements and future research challenges," *Int. J. Rail Transp.*, vol. 6, no. 2, pp. 57–82, Apr. 2018.

[18] C. Sanchez-Rebollo, J. R. Jimenez-Octavio, and A. Carnicero, "Active control strategy on a catenary–pantograph validated model," *Vehicle Syst. Dyn.*, vol. 51, no. 4, pp. 554–569, Apr. 2013.

[19] A. Mitsuo, I. Mitsuru, and N. Sei, "Analyses of contact force fluctuation between catenary and pantograph," *Quart. Rep. RTRI*, vol. 41, no. 4, pp. 30–38, 2000.

[20] X. Lu, Z. Liu, J. Zhang, H. Wang, Y. Song, and F. Duan, "Prior-information-based finite-frequency H_∞ control for active double pantograph in high-speed railway," *IEEE Trans. Veh. Technol.*, vol. 66, no. 10, pp. 8723–8733, Oct. 2017.

[21] H. Wang, Z. Liu, A. Núñez, and R. Dollevoet, "Entropy-based local irregularity detection for high-speed railway catenaries with frequent inspections," *IEEE Trans. Instrum. Meas.*, vol. 68, no. 10, pp. 3536–3547, Oct. 2019.

[22] Y. Song, Z. Wang, Z. Liu, and R. Wang, "A spatial coupling model to study dynamic performance of pantograph-catenary with vehicle-track excitation," *Mech. Syst. Signal Process.*, vol. 151, pp. 1–26, Apr. 2021.
[23] T. Wu and M. Brennan, "Dynamic stiffness of a railway overhead wire system and its effect on pantograph–catenary system dynamics," *J. Sound Vib.*, vol. 219, no. 3, pp. 483–500, 1999.
[24] M. Simarro, S. Postigo, J. A. Cabrera, and J. J. Castillo, "A procedure for validating rigid catenary models using evolutionary techniques," *Comput. Struct.*, vol. 228, pp. 106145–106155, Feb. 2020.
[25] Y. Song, H. Wang, and Z. Liu, "An investigation on the current collection quality of railway pantograph-catenary systems with contact wire wear degradations," *IEEE Trans. Instrum. Meas.*, vol. 70, pp. 1–11, 2021.
[26] *Railway Applications—Current Collection Systems—Validation of Simulation of the Dynamic Interaction Between Pantograph and Overhead Contact Line*, Standard EN 50318, European Committee for Electrotechnical Standardization, Brussels, Belgium, 2018.
[27] J. Guan, J. Wu, Y. Zhong, and J. Zhang, "Reference significance of European railway technical specifications for China's pantograph and catenary standards," *China Railway*, vol. 620, no. 2, pp. 76–80, Feb. 2014.
[28] Y. Hou, "Research on the vibration performane of electrified railway catenary under double pantograph current collection," Ph.D. thesis, Southwest Jiaotong Univ., Chengdu, China, 2014.
[29] J. Wang, Z. Tian, and J. Li, "Study of the influence of current-receiving quality between pantograph and OCS from tensile force acting on catenary wire," *J. China Railway Soc.*, vol. 27, no. 1, pp. 114–118, Feb. 2005.
[30] H. Li and Z. Tian, "Research on the rigid suspension plane layout of overhead contact systems," *J. Railways*, vol. 43, no. 2, pp. 103–106, Apr. 2003.
[31] Y. Song, Z. Liu, F. Duan, Z. Xu, and X. Lu, "Wave propagation analysis in high-speed railway catenary system subjected to a moving pantograph," *Appl. Math. Model.*, vol. 59, pp. 20–38, Jul. 2018.
[32] J. Guan, "Study on dynamic interaction between pantograph and overhead conductor rail," Ph.D. thesis, Southwest Jiaotong Univ., Chengdu, China, 2016.

YING WANG received the B.S. degree from the School of Electrical Engineering and Automation, Chongqing University, Chongqing, China, and the Ph.D. degree from the School of Electrical Engineering, Southwest Jiaotong University, Chengdu, China. His current research interests include high-power converters and harmonics compensation.

QIANG HUANG received the B.S. degree from the School of Electrical Engineering and Automation, Lanzhou Jiaotong University, Lanzhou, China, in 2020, where he is currently pursuing the M.S. degree in electrical engineering. His current research interests include electrical contact and the dynamic performance of pantograph-catenary.

XIAOQIANG CHEN received the Ph.D. degree from the School of Electrical Engineering and Automation, Lanzhou Jiaotong University, Lanzhou, in 2010. He is currently a Professor with the School of Electrical Engineering and Automation, Lanzhou Jiaotong University. His current research interests include high-power special-type power supplies and their application and energy storage systems.

GANGHUI ZHAO received the B.S. degree from the School of Electrical Engineering and Automation, Lanzhou Jiaotong University, Lanzhou, China, in 2020, where he is currently pursuing the M.S. degree in electrical engineering. His current research interests include electrical contact and the dynamic performance of pantograph-catenary.

XIUQING MU received the M.S. degree from the Department of Electrical Engineering and Automation, Xihua University, Chengdu, China, in 2011. She is currently pursuing the Ph.D. degree in electrical engineering with Lanzhou Jiaotong University, China. Her current research interests include stability analysis and control of electrified railway vehicle network coupling systems.